International Journal of Multiphase Flow 35 (2009) 312–322

Contents lists available at ScienceDirect

International Journal of Multiphase Flow

journal homepage: www.elsevier.com/locate/ijmulflow

Freely rising light solid spheres

C.H.J. Veldhuis [a,*], A. Biesheuvel [b], D. Lohse [a]

[a] Physics of Fluids Group, Department of Science and Technology, J.M. Burgers Centre for Fluid Mechanics, and Impact Institute, Meander Building, University of Twente, P.O. Box 217, 7500AE Enschede, The Netherlands

[b] Institute des Sciences et Techniques de l'Ingénieur de Lyon, Université Claude Bernard Lyon 1, and Laboratoire de Mécanique des Fluides et d'Acoustique, Ecole Centrale de Lyon, Lyon, France

ARTICLE INFO

Article history:
Received 29 October 2007
Received in revised form 13 January 2009
Accepted 19 January 2009
Available online 29 January 2009

ABSTRACT

This paper examines the behavior of spheres rising freely in a Newtonian fluid when the ratio between the density of the spheres and that of the surrounding fluid is about 0.02. High-speed imaging is used to reconstruct three-dimensional trajectories of the rising spheres. From the analysis of the trajectories the magnitudes of the drag and lift forces exerted by the surrounding fluid are deduced. It is argued that the two main contributions to the drag force are (i) a viscous drag that may be estimated from the standard drag curve by evaluating the Reynolds number using the actual value of the velocity, and (ii) an inertial drag that arises essentially by the same mechanisms that cause the lift-induced drag familiar from wing theory. Estimates of both contributions, the latter using visualizations of the wakes of the spheres, give a favorable agreement with the measured drag forces. These findings are closely related to recent numerical results in the literature on the forces experienced by oblate ellipsoidal bubbles rising in quiescent water.

1. Introduction

The mean velocity of single solid spheres, rising or falling freely in an infinite fluid, is of interest in numerous fields, including chemical, mechanical, and environmental engineering. This velocity may be determined from a balance between the net gravitational force and the mean drag on the sphere,

$$\frac{1}{6}\pi d^3|\rho_s-\rho|g=\frac{1}{8}\pi d^2\rho U_T^2 C_D, \tag{1}$$

together with a relation for the drag coefficient C_D as a function of the Reynolds number $Re = U_T d/\nu$. Here ρ_s, d, and U_T denote the density, diameter, and mean velocity of the sphere, respectively, ρ and ν are the density and the kinematic viscosity of the surrounding fluid, and g is the gravitational acceleration. A simple and well-known relation for the drag coefficient of spheres is that of Turton and Levenspiel (1986),

$$C_D=\frac{24\left(1+0.173Re^{0.657}\right)}{Re}+\frac{0.413}{1+16300Re^{-1.09}}; \tag{2}$$

a discussion of this relation and of others, together with a proposal for an alternative

$$C_D=\frac{24}{Re}\left(1+0.150Re^{0.681}\right)+\frac{0.407}{1+8710Re^{-1}}, \tag{3}$$

is given in Brown and Lawler (2003). Both relations are applicable for $Re < 2\times10^5$ and based on data from spheres held fixed in space and falling spheres.

The data used to construct these relations do not include cases in which the density ratio ρ_s/ρ is small (on which we will focus in this paper), as then the particles do not rise straight and relations (2) and (3) are no longer applicable. Based on on experiments with 'light' solid spheres rising in water (Karamanev and Nikolov, 1992, 1996) and soap bubbles filled with helium or hydrogen rising in air (Karamanev, 2001), the ratio $\rho_s/\rho < 0.3$ has been suggested as threshold of applicability of above equations. For these small density ratios and for $Re > 130$ Karamanev and co-workers suggest the constant value $C_D = 0.95$ instead.[1]

For the light spheres which do not rise straight the simplistic Eqs. (2) and (3) must be replaced by a more detailed force balance analysis in the co-moving Frenet reference system of the sphere itself, as e.g., done by Shew et al. (2006) or very recently by Fernandes et al. (2008). This analysis goes back already to Kirchhoff and for completeness is repeated in Section 3.3, to allow for an extraction of drag and lift forces for the spiraling light sphere.

The wake structures behind spheres has been studied for a long time. Much of this research is related to spheres held fixed in space (e.g., Schouveiler and Provansal, 2002, 1999). It is well-known that the wake behind fixed spheres looses its axi-symmetry at $Re = 212$; the wake now consists of two stable vortex threads. At

---

* Corresponding author. Tel.: +31 317 49 3374.
E-mail addresses: c.veldhuis@marin.nl (C.H.J. Veldhuis), d.lohse@utwente.nl (D. Lohse).

[1] This may be compared with the much smaller limiting value for high Reynolds numbers following from Eqs. (2) and (3), namely $C_D = 0.413$ and $C_D = 0.407$, respectively, that is found for heavy spheres.

0301-9322/$ - see front matter © 2009 Elsevier Ltd. All rights reserved.
doi:10.1016/j.ijmultiphaseflow.2009.01.005

$Re = 270$ these threads become unstable and low amplitude undulations set in. At $Re \approx 345$ the two continuous vortex structure break up and a vortex shedding mechanism takes over. For freely moving spheres the literature is less extensive; Magarvey and MacLatchy (1965) show beautiful wake structures behind falling spheres visualized with dye injection. The structures behind these falling spheres are similar to those observed behind spheres held fixed in space. Lunde and Perkins (1997) used a similar dye injection method to investigated the wake of ellipsoidal polystyrene particles rising in water; they observe a highly unstable wake in which the double vortex threaded wake structure is not visible. They show that large amounts of vorticity are shed for zigzagging particles at the outer positions of the zigzag trajectory; indicating the influence of the wake on the path of the particle, and vice versa. More recently Veldhuis et al. (2005) investigated the wake structures behind rising and falling spheres at high Reynolds numbers in more detail. They showed that the wake structure and its influence on the sphere motion strongly depends on the density ratio; e.g., a falling sphere with a density 5% more than that of water clearly shows periodic vortex shedding without the sphere path being influenced. Whereas the path of a rising sphere with a density 5% less than that of water shows periodic fluctuations equal to the fluctuations in the wake of the sphere. In a reaction on numerical work by Jenny et al. (2004) and Veldhuis and Biesheuvel (2007) investigated the behavior of rising and falling spheres experimentally in a larger range of density ratios, sphere diameters, and viscosity. They found regions with low and high frequency wake and path oscillations, and a region in which the motion of the sphere becomes chaotic. The 'light' rising spheres of Karamanev and co-workers are part of this chaotic regime. As Jenny et al. (2004) found in their numerical paper, Veldhuis and Biesheuvel (2007) also found clear differences between the wakes and motions of falling and rising. The strong influence of the wake for lower density ratios has also been reported by Mougin and Magnaudet (2006) in their numerical study of rising bubbles. They calculated the time dependent forces experienced by the bubble and showed that the wake behind an oblate ellipsoidal bubble gives rise to a 30% increase of the drag experienced by the bubble compared to drag calculated from potential flow (Levich drag). Although there is a difference in shape between a sphere and an ellipsoidal bubble and also a difference in boundary condition (no-slip versus no-shear, respectively), resulting in a different vorticity production, we might ask ourselves if a similar mechanism is at work for light rising spheres.

To examine the questions raised by the work of Karamanev et al. (1996) and Mougin and Magnaudet (2006), we have carried out further experiments on the behavior of light ascending solid spheres. A brief description of the materials and methods is given in Section 2, followed by a discussion of the drag relation in Section 3. The trajectories of the light spheres ($\rho_s/\rho \approx 0.02$) have been analyzed to deduce the forces exerted by the surrounding fluid; the results are presented at the end of Section 3, together with a simple model for the drag experienced by the spheres. In Section 4 we discuss our results and compare those with the literature. The paper ends with conclusions.

2. Materials and methods

For the experiments we used a plexiglass tank with a height of 0.50 m and a cross-section of 0.15 m × 0.15 m, filled with decarbonated tap water. The temperature was maintained at a temperature of 21 °C ± 0.2, giving a fluid density of 998 $\text{kg m}^{-3} \pm 0.05$ and a kinematic viscosity of $0.96 \times 10^{-6}\ \text{m}^2\ \text{s}^{-1} \pm 0.5 \times 10^{-8}$. A total of 31 experiments with light solid spheres were conducted. We used expanded-polystyrene (EPS) spheres, density $\rho_s = 18.5\ \text{kg m}^{-3} \pm 1.5$, each with a different diameter in a range between 3.5 and 5.6 mm ± 0.1. In addition, to see any differences in their dynamics, experiments with ascending and falling spheres with larger density were carried out. These included spheres of the following materials and properties: polypropylene ($\rho_s = 850\ \text{kg m}^{-3}, d = 3.97$ mm); low-density polyethylene ($\rho_s = 925\ \text{kg m}^{-3}, d = 6.35$ mm and $d = 7.94$ mm); polystyrene ($\rho_s = 1058\ \text{kg m}^{-3}, d = 3.97$ mm); polyamide-imide ($\rho_s = 1410\ \text{kg m}^{-3}, d = 3.18$ mm and $d = 3.97$ mm); and glass ($\rho_s = 2472\ \text{kg m}^{-3}, d = 2.50$ mm; $\rho_s = 2629\ \text{kg m}^{-3}, d = 4.00$ mm). The error for all diameters within this set is ± 0.01 mm and for the density $\pm 5\ \text{kg m}^{-3}$; the sphericity of the spheres is at least 0.99.

In a second series of experiments the water was heated from above. This resulted in a small temperature gradient of 1.0 K/cm, which allows to use a Schlieren-optics technique to visualize the wakes of the spheres. This technique was originally developed to obtain information on the wakes behind gas bubbles (de Vries et al., 2002). More details of the improved set-up used here may be found in Veldhuis et al. (2005) and Veldhuis and Biesheuvel (2007).

According to numerical work by Jenny et al. (2004) it can take several hundreds of sphere diameters before a sphere reaches its final stage of motion. Before this stage the sphere can move along non-reproducible paths. In order to verify whether the spheres have reached their final stage of motion we performed a third series of experiments in a large water tank (diameter 16 cm, length 2.5 m). Two mutually perpendicular views of the spheres are recorded over a distance of 40 cm, 2 m after release of the sphere. This results in a larger field of view; therefore the spatial resolution of this recording method is smaller: 0.9 mm pixel^{-1}, and so is the temporal resolution. The smaller resolution gives rise to larger errors in the reconstruction of the paths and forces. Therefore this method is mainly used to verify the general behavior of the spheres. In the discussion in Section 4 we will give some results obtained with the large setup. The small setup, with higher resolution, is used for detailed analysis of the forces and the drag coefficient. The results presented in the next section are obtained using this setup.

3. Experimental results

3.1. The drag relation

The data for the dimensionless mean velocity U_T, i.e., the Reynolds number

$$Re = \frac{U_T d}{\nu}, \tag{4}$$

and the drag coefficient as defined by Eq. (1),

$$C_D = \frac{4}{3}|\rho_s/\rho - 1| g d / U_T^2. \tag{5}$$

have been compiled in Fig. 1. The 'light' ascending spheres ($\rho_s/\rho \approx 0.02$) are distinguished from the 'heavy' ascending spheres ($0.3 \lesssim \rho_s/\rho < 1.0$) by the use of the colors red (light) and green (heavy); the data for settling spheres ($\rho_s/\rho > 1.0$) are indicated in blue. The error-bars represent estimates of the uncertainty in the determination of the physical parameters in each individual experiment. The solid curve is the relation (2) proposed by Turton and Levenspiel (1986) and the dashed line is the relation for light spheres, $C_D = 0.95$ for $Re > 130$, proposed by Karamanev and Nikolov (1992).

The figure confirms what was observed by Karamanev's group, namely that as the density ratio ρ_s/ρ is sufficiently small and the Reynolds number is sufficiently high, due to the resulting spiraling there are significant deviations from the standard drag relation applicable for spheres falling or rising straight. However, the measured values of the drag coefficient for our light spheres, all

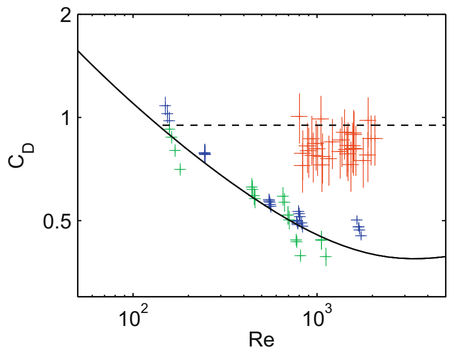

Fig. 1. The drag coefficient C_D, defined by (5), as a function of the Reynolds number *Re*, based on the mean velocity of rise U_T. Solid curve: Turton–Levenspiel relation for heavy spheres ($\rho_s/\rho > 0.3$). Dashed line: Karamanev–Nikolov relation for light spheres ($\rho_s/\rho < 0.3$). Color: experimental data with error-bars indicating the maximum experimental error. Blue: $\rho_s/\rho > 1.0$; green $0.3 < \rho_s/\rho < 1.0$ – both data sets basically agree with the standard drag curve within the precision we can achieve. Red: $\rho_s/\rho = 0.02$, black: $\rho_s/\rho = 0.02$ in large water tank. (For interpretation of the references to color in this figure legend, the reader is referred to the web version of this paper.)

for Reynolds numbers much higher than 130, are lower than the proposed value $C_D = 0.95$.

Jenny et al. (2003) have recently shown by numerical analysis that the critical Reynolds number Re_{cr} at which the flow around a 'free' massless solid sphere looses axial symmetry is 205.8, a value that is only slightly lower than the well-known critical value $Re_{cr} = 211.9$ for the flow around a fixed sphere (in other words, an extremely heavy 'free' sphere). This suggests that the Karamanev & Nikolov's 'critical' Reynolds number of 130 is merely the value of the Reynolds number for which the Turton–Levenspiel relation gives $C_D(Re) = 0.95$.

3.2. Trajectories followed by light spheres

Fig. 2 shows the 3D path followed by the spheres, as they are reconstructed from the two perpendicular side-views, for six representative experiments. For all experiments the density ratio $\rho_s/\rho \simeq 0.02$ and the diameters range from 3.4 mm to 5.8 mm, so that the Galileo number *G* has values between 615 and 1712. The Reynolds number based on the mean velocity of rise increases from 889 to 1982; detailed information is given in the caption of the

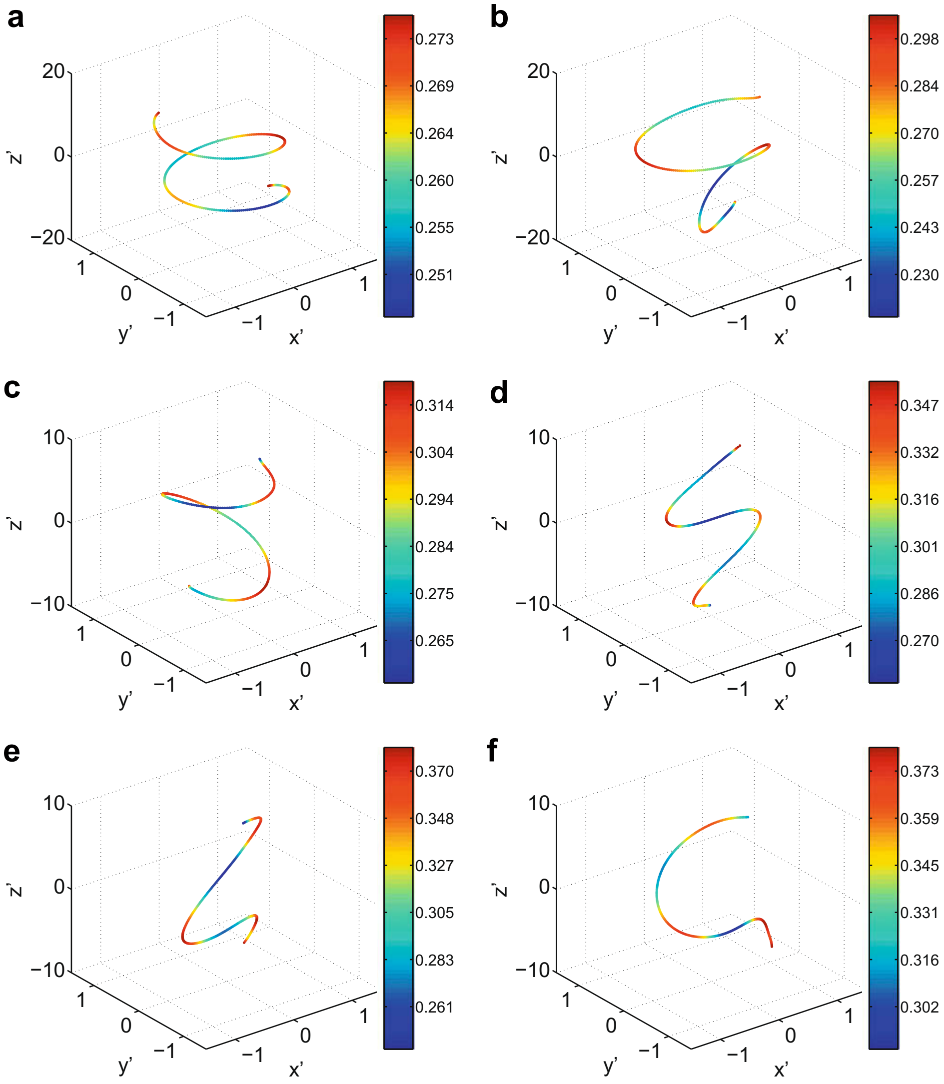

Fig. 2. Measured trajectories of spheres rising in water; origin of frame is located at the position where the spheres enters the water tank. The color values represent the tangential velocity of the spheres, with the numbers next to the color codes giving the corresponding value in m s^{-1}. Spatial coordinates have been non-dimensionalized with the diameter of the spheres. In all cases $\rho_s/\rho \simeq 0.02$. (a) $d = 3.4$ mm, $G = 615$; (b) $d = 3.9$ mm, $G = 756$; (c) $d = 4.3$ mm, $G = 875$; (d) $d = 4.8$ mm, $G = 1032$; (e) $d = 5.4$ mm, $G = 1231$; (f) $d = 5.7$ mm, $G = 1335$. (For interpretation of the references to color in this figure legend, the reader is referred to the web version of this paper.)

figure. The character of these trajectories is revealed more clearly by a projection on a horizontal plane, i.e., as if the spheres were observed from above. These views are given in Fig. 3. Colors are used to indicate the tangential velocity of the spheres, the numbers next to the color giving the corresponding value in ms^{-1}. The velocity has the highest value where the path is most strongly curved. The variations in the velocity are largest when the path is close to a perfect zigzag (see the color codes), and least when the path is nearly a pure helix (spheres following a perfect helicoidal path do this at a constant velocity).

3.3. Drag and lift forces

To determine the forces experienced by the spheres it is helpful to use a Frenet reference frame, i.e., a moving orthogonal frame with the tangent to the curve **t**, the normal to the curve **n**, and the binormal **b** as unit vectors, similarly as done by Shew et al. (2006) or Fernandes et al. (2008). We chose this frame, because we are interested in the actual drag, which acts in tangential direction and not in time averaged drag in vertical direction. Later on we will see that the advantage of the choice for the normal and binormal vectors is that the forces in the case of a pure helix become constant. Furthermore, the binormal will be discontinuous for a zigzag at the position where the sphere crosses the centerline of the zigzag; this makes it easier to interpret the time dependent force data as we will see in Fig. 4.

Let $\mathbf{r}(t)$ denote the time-dependent position vector of the center of the sphere with respect to a fixed reference frame and let $s(t)$ measure the distance travelled along the curve from some arbitrary initial instant. Then the unit vectors are defined as

$$\mathbf{t}=\frac{d\mathbf{r}}{ds},\qquad \mathbf{n}=\frac{d\mathbf{t}}{ds}\Big/\left|\frac{d\mathbf{t}}{ds}\right|,\qquad \mathbf{b}=\mathbf{t}\times\mathbf{n}, \tag{6}$$

while the variation of these unit vectors along the curve is given by the Frenet–Serret formulae

$$\frac{d\mathbf{t}}{ds}=\kappa\mathbf{n},\qquad \frac{d\mathbf{n}}{ds}=-\kappa\mathbf{t}+\tau\mathbf{b},\qquad \frac{d\mathbf{b}}{ds}=-\tau\mathbf{n}. \tag{7}$$

Here κ is the curvature and τ is the torsion of the curve. An instructive, alternative formulation is obtained on introducing the Darboux vector

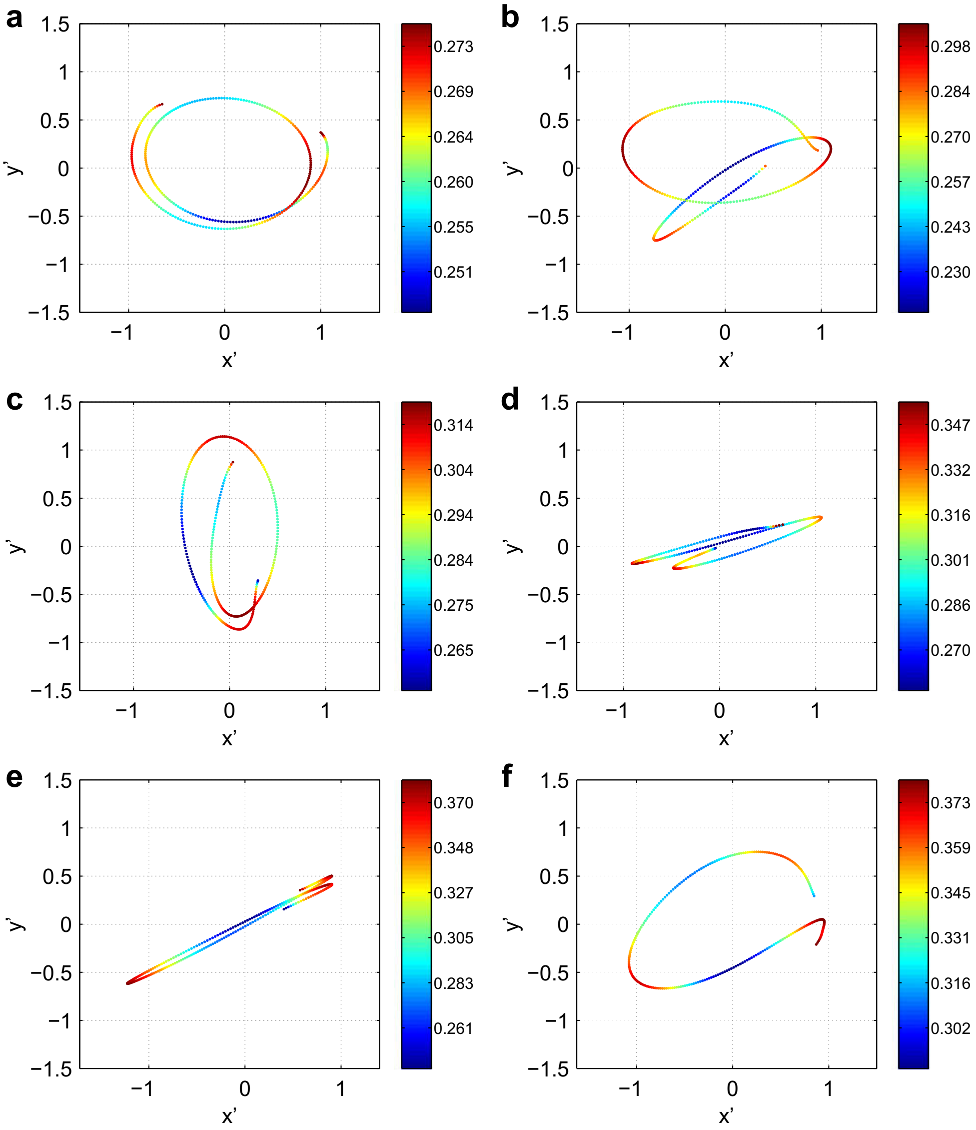

Fig. 3. Projection of the six measured sphere trajectories of Fig. 2 on the *XY*-plane. Further details are given in the caption of Fig. 2. (For interpretation of the references to color in this figure legend, the reader is referred to the web version of this paper.)

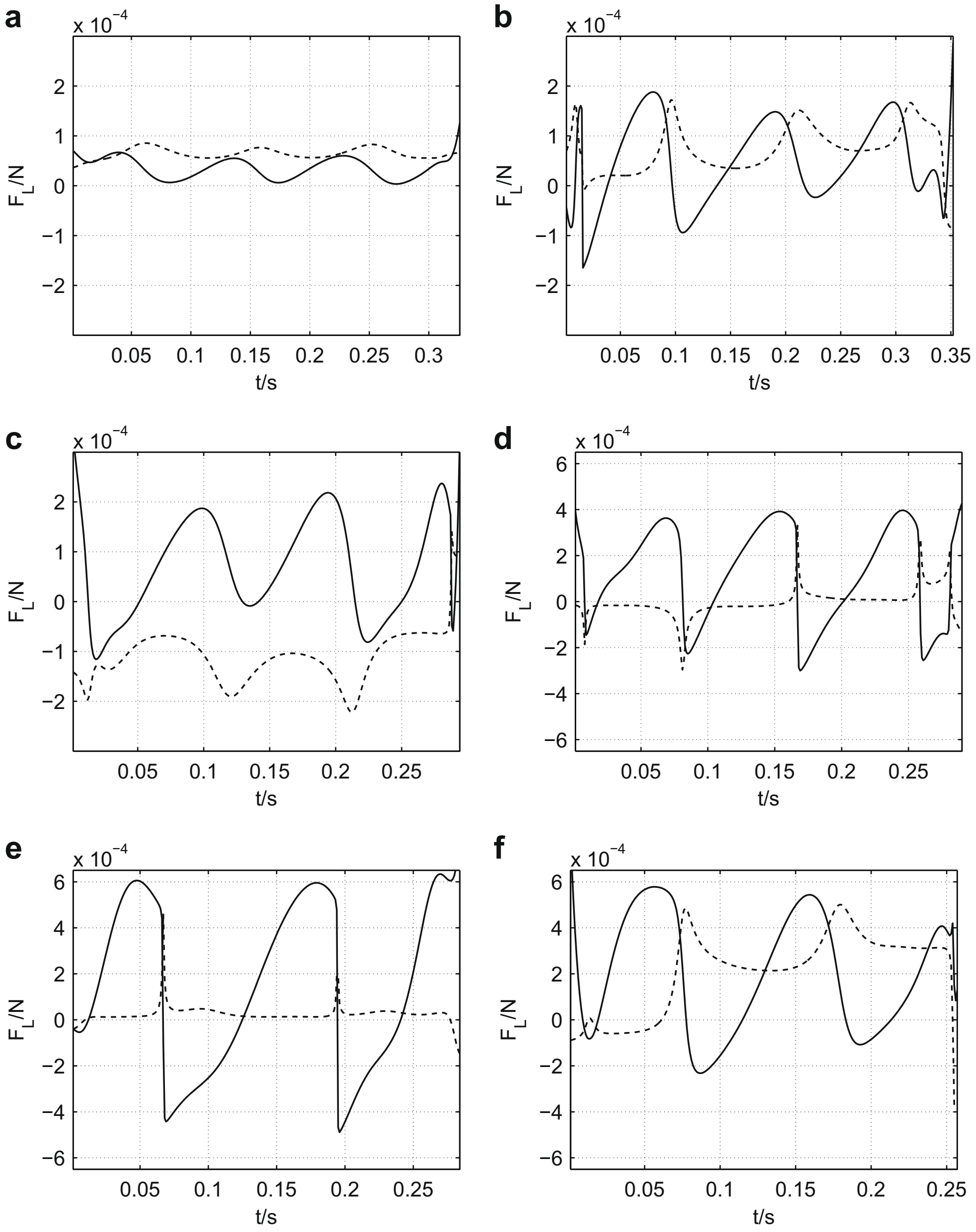

Fig. 4. The components of the lift force acting on the spheres. Solid line: component in the direction of the normal to the curve (F_n). Dashed line: component in the direction of the binormal to the curve (F_b). Further details as in the caption of Fig. 2.

$$\mathbf{d} = \tau\mathbf{t} + \kappa\mathbf{b}, \tag{8}$$

by which the Frenet–Serret formulae become

$$\frac{\mathrm{d}\mathbf{t}}{\mathrm{d}s} = \mathbf{d}\times\mathbf{t}, \quad \frac{\mathrm{d}\mathbf{n}}{\mathrm{d}s} = \mathbf{d}\times\mathbf{n}, \quad \frac{\mathrm{d}\mathbf{b}}{\mathrm{d}s} = \mathbf{d}\times\mathbf{b}. \tag{9}$$

Hence, the variation of the unit vectors consists of a rotation around the instantaneous tangent and binormal at rates τ and κ, respectively.

The linear momentum of the body is expressed with respect to the Frenet frame, the motion of which is described by the translational velocity

$$\mathbf{U} = \frac{\mathrm{d}s}{\mathrm{d}t}\mathbf{t} \tag{10}$$

of the origin, and the angular velocity

$$\mathbf{\Omega} = \frac{\mathrm{d}s}{\mathrm{d}t}(\tau\mathbf{t} + \kappa\mathbf{b}) \tag{11}$$

about the instantaneous position of its axes. The momentum equation of the body is deduced from the Kirchhoff equations (see also Mougin and Magnaudet, 2002a) and reads

$$\left(\frac{\mathrm{d}\mathbf{I}}{\mathrm{d}t}\right)_F + \mathbf{\Omega}\times\mathbf{I} = \{1-(\rho/\rho_s)\}M\mathbf{g} + \mathbf{F}, \tag{12}$$

where the first term on the left-hand side is the vector formed by the rates of change of the components of the virtual momentum I of the body with respect to the Frenet reference frame. The virtual momentum of the body is the sum of the actual momentum of the body and the impulse of the irrotational fluid motion that would result if the motion of the body would be generated instantaneously from a state of rest. The first term on the right-hand side is the gravitational force, with M the mass of the sphere. The ‘extraneous’ force **F** is what Lighthill (1986) calls ‘the vortex-flow force’, i.e., that part of the force which the fluid exerts on the body due to the presence of ‘additional vorticity’ in the flow. It may be noted that expressions in terms of the *actual* vorticity distribution in the flow have been given by Kambe (1987) and Howe (1995); connections with earlier work of J. M. Burgers are discussed in Biesheuvel and Hagmeijer (2006). The components of the vortex-flow force (F_X, F_Y, F_Z) may be determined from the experimental data on the trajectory $\mathbf{r}(t)$, and may subsequently be projected on the Frenet frame to obtain (F_t, F_n, F_b). The drag force on the sphere is $\mathbf{F}_D = -F_t\mathbf{t}$ and the lift force is given by $\mathbf{F}_L = F_n\mathbf{n} + F_b\mathbf{b}$. Here we approximate the rate of change of the virtual momentum by the value it would have in a stationary fluid,

$$\left(\frac{\mathrm{d}\mathbf{I}}{\mathrm{d}t}\right)_F = \left\{1 + \frac{1}{2}(\rho/\rho_s)\right\} M \frac{\mathrm{d}^2 s}{\mathrm{d}t^2}\mathbf{t}. \tag{13}$$

Hence, conservation of linear momentum of the body is described with respect to a Frenet reference frame by the three equations

$$\left\{1 + \frac{1}{2}(\rho/\rho_s)\right\} M \frac{\mathrm{d}^2 s}{\mathrm{d}t^2} - \{1 - (\rho/\rho_s)\} M g_t = F_t, \tag{14}$$

$$\left\{1 + \frac{1}{2}(\rho/\rho_s)\right\} M \kappa \left(\frac{\mathrm{d}s}{\mathrm{d}t}\right)^2 - \{1 - (\rho/\rho_s)\} M g_n = F_n, \tag{15}$$

$$-\{1 - (\rho/\rho_s)\} M g_b = F_b. \tag{16}$$

Time-traces of the components (F_n, F_b) of the lift force are shown in Fig. 4, negative values of F_n indicating that this component is directed away from the center of curvature. Fig. 5 shows the drag force F_D (solid line); the other lines will be discussed in Section 3.4. In both cases we see that the forces are steady for helicoidal motion. Here we have again assumed that the liquid around the rising sphere is stationary and the drag therefore still aligned with the particle motion.

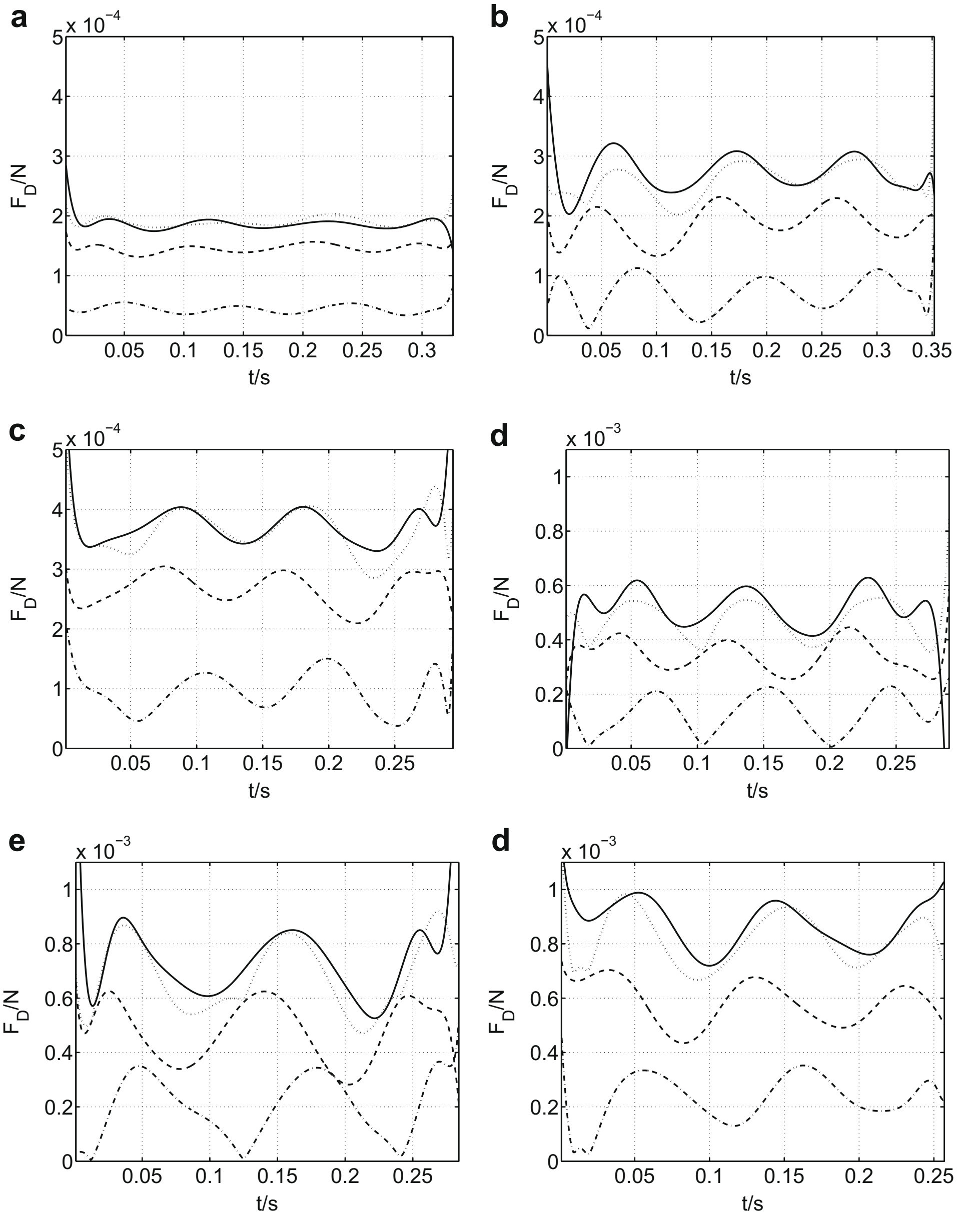

Fig. 5. Analysis of the drag forces acting on spheres. Solid curves: measured drag force; dashed curves: viscous drag as given by the Turton-Levenspiel relation with the Reynolds number based on the instantaneous velocity; dashed-dotted curves: estimates of the lift induced drag; dotted curves: drag force as a combination of viscous drag and lift-induced drag. Parameters as given in the caption of Fig. 2.

For what concerns the lift forces, the origin of a force transverse to the direction of motion of the spheres is the *generation* of a vorticity distribution in the fluid with a hydrodynamic impulse that has a component normal to the direction of the flow. Visualizations of the wakes of solid spheres by Veldhuis et al. (2005) provided clear evidence of the continuous generation of such vorticity distributions with a structure which in the near wake consists of two parallel vortex threads, each with a strong axial component of vorticity (in opposite directions). Zigzagging and spiralling bubbles also have such a 'bifid wake', as shown in de Vries et al. (2002) and Mougin and Magnaudet (2002b). Similar vortex structures are found some distance behind the wings of an airplane. At relatively low Reynolds numbers this bifid wake structure may extend a considerable distance downstream of the solid spheres (or bubbles). The threads may develop kinks and connect at fairly regularly spaced positions. At higher Reynolds numbers ($Re > 800$) the wake becomes unstable and even turbulent already close to the body; the experiments presented in this section are in this regime. These instabilities may involve a vigorous redistribution of the vorticity already present in the flow, yet the generation of new vorticity, i.e., the addition of hydrodynamic impulse transverse to the direction of motion of the body, varies much more smoothly, as evidenced by the results for the lift forces of the present experiments.

3.4. The nature of the drag

A simple method to estimate the drag forces experienced by the spheres is to use the Turton–Levenspiel relation (2) with the Reynolds number based on the instantaneous velocity $U(t)$ of the spheres. This procedure is similar to that suggested in Lighthill (1986). It leads to rather unsatisfactory results, as may be seen from Fig. 5, which also shows time-traces of the drag calculated in this way (the dashed curve): the actual drag is not only larger, but also shows a time-lag with respect to the calculated drag. A possibly remedy, proposed, for example, by Sarpkaya (2001), is to modify the added mass coefficient $\frac{1}{2}(\rho/\rho_s)M$ on the grounds that this potential-flow concept needs adjustment to reflect the presence of vorticity in the flow and/or the action of viscosity. This approach is not appealing considering the nature of the vortex-flow force, as was explained clearly by Lighthill (1986) and more recently by Leonard and Roshko (2001); it is well-established that added mass is fully determined by potential flow concepts and needs no correction for the contribution of vorticity.

Fig. 6 shows the drag, lift, and velocity of the zigzagging sphere from sub-figure (e) of the previous figures. We clearly see that the drag force and the velocity of the sphere are out-of-phase. Any estimate of the drag force according to relation (2) will be in-phase with the velocity and will therefore not give a correct estimate of the actual drag force. A phase shift towards the actual drag can be established by also taking into account the effect of the lift force; this approach to drag will be discussed below.

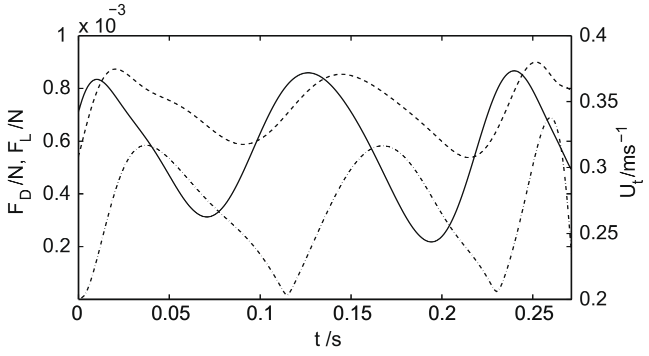

Fig. 6. - - - - -, Drag force; and -·-, lift force (left axis), and ——, tangential velocity (right axis) for the sphere from the previous sub-figure (e).

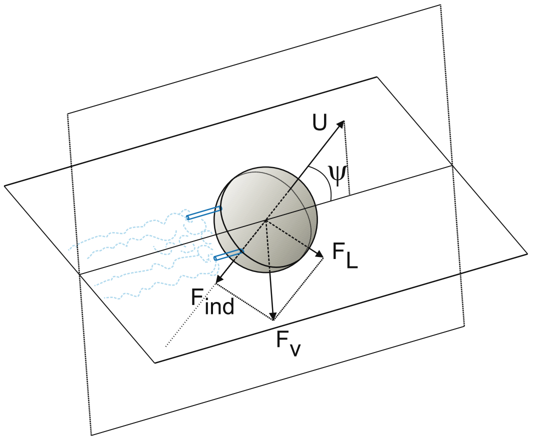

Fig. 7. Because of the continuous generation of new vorticity, which close to the body consists of two parallel vortex threads, each with a strong axial component of vorticity but in opposite directions, a sphere experiences a vortex-flow force F_v at right angles to a plane through the two vortex threads. This force may be decomposed in a lift force F_L normal to the direction of motion and a lift-induced drag F_{ind} opposite to the direction of motion of the sphere.

It is better to view relation (2) as giving a good estimate of the viscous contribution to the vortex-flow force, while an estimate of the true drag follows from adding a (predominantly inertial) contribution, which in wing theory is referred to as the 'lift-induced drag'. This contribution, as illustrated in Fig. 7, arises essentially because the instantaneous force, $\mathbf{F}_v$, associated with the generation of a vorticity structure which near the body consists of two vortex threads with oppositely directed axial vorticity, is not at right angles with the instantaneous direction of motion of the sphere. Hence, the lift-induced drag arises because the instantaneous direction of motion is not parallel to the plane through the two threads at the place of origin of these threads. If the angle between the velocity vector and that plane is ψ, then the true force that results from the generation of the vortex threads is directed normal to that plane and has magnitude

$$(F_n^2 + F_b^2)^{\frac{1}{2}}/\cos\psi.$$

It may be decomposed into components in the directions $\mathbf{n}$ and $\mathbf{b}$ with magnitudes F_n and F_b, respectively, which have been

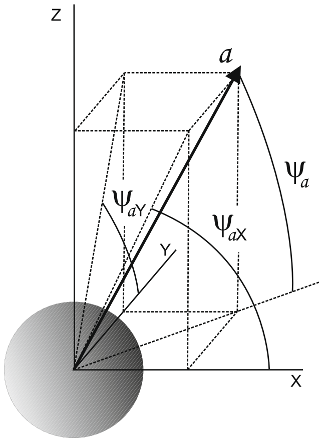

Fig. 8. The angle between the vector **a** and the horizontal *XY*-plane is called ψ_a. The angles with the horizontal in projections on the *XZ*-plane and *YZ*-plane are ψ_{aX} and ψ_{aY}, respectively. Eq. (19) gives a relation between these three angles.

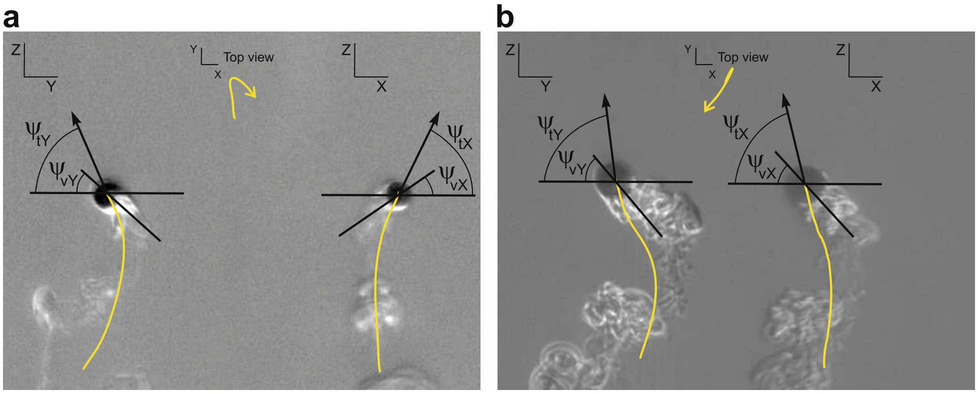

Fig. 9. Schlieren visualizations of the wake of rising spheres, viewed from two orthogonal directions. The yellow line indicates the path followed by the sphere during the time interval t between the moment of entering the field-of-view and the moment that the picture was taken. The angles ψ_{tX} and ψ_{tY} are the angles between the direction of motion and the horizontal as observed in projections on the XZ-plane and YZ-plane ; similarly, ψ_{vX} and ψ_{vY} are the estimated angles between the horizontal and the plane containing the two vortex threads. (a) $\rho_s/\rho \simeq 0.02, d = 3.7$ mm, $G \simeq 775, t = 0.125$ s; (b) $\rho_s/\rho \simeq 0.02, d = 5.8$ mm, $G \simeq 1712, t = 0.110$ s. With time t the time passed from the moment the sphere path is plotted. (For interpretation of the references to color in this figure legend, the reader is referred to the web version of this paper.)

determined experimentally, and a further component in the direction opposite to the tangent **t** with magnitude

$$F_{ind} = (F_n^2 + F_b^2)^{\frac{1}{2}} \tan\psi. \tag{17}$$

Let ψ_t be the angle between the tangent to the trajectory and the horizontal plane, and similarly let ψ_v be the angle between the 'vortex-plane' and the horizontal plane. Hence the angle ψ between the velocity vector and the vortex-plane is given by

$$\psi = \psi_v - \psi_t. \tag{18}$$

We now define the angle between the vector **a** and the horizontal XY-plane as ψ_a, see Fig. 8. The angles with the horizontal in projections on the XZ-plane and YZ-plane are called ψ_{aX} and ψ_{aY}, respectively. From elementary geometry one then obtains

$$\frac{1}{\tan^2\psi_a} = \frac{1}{\tan^2\psi_{aX}} + \frac{1}{\tan^2\psi_{aY}}. \tag{19}$$

We have tried to obtain information on the time-variation of the angle ψ from flow visualizations made with our Schlieren-optics set-up. Two examples of Schlieren visualizations of the wakes of rising solid spheres are shown in Fig. 9, in which we have indicated the angles $\psi_{tX}, \psi_{vX}, \psi_{tY}$, and ψ_{vY}; the values of ρ_s/ρ and G are based on the measured temperature at the center of the field-of-view. Obviously, this procedure can only yield rough estimates of ψ_{vX} and ψ_{vY}, because the turbulence in the wake makes the pictures 'blurry' and the wakes are highly 'curved'. Furthermore, the angle ψ is best calculated when the sphere crosses the centerline of the zigzag, where the path is (almost) straight. Now the vorticity structure is also straight, enabling a good prediction of the angle ψ. For a typical Schlieren experiment this results in two or three measurement points per experiments for the angle ψ, approximately one every 0.1 s. On using Eqs. (18) and (19) we obtain $\psi = 26.1^\circ \pm 1$ for the case shown in Fig. 9(a) and $\psi = 37.5^\circ \pm 1$ for that in Fig. 9(b). From a whole range of visualizations for values of G between 600 and 1800 it appears that along the sphere trajectories the angle ψ varies roughly between 25° to 38°. Given the uncertainty in determining the variation of ψ with time, and in order to have some definite value, we chose a fixed angle $\psi = 30^\circ$ and used this to evaluate expression (17).[2] This procedure gives the dashed-dotted curves shown in Fig. 5 (which in this case is just $\frac{1}{3}\sqrt{3}$ times the magnitude of the lift force). Finally, adding the lift-induced contribution to the viscous contribution as estimated from the relation (2), results in an estimate of the drag experienced by the spheres that is presented in Fig. 5 as the dotted curves. The agreement with the measured drag (the solid curves) turns out to be excellent. This supports our view of the mechanisms that govern the generation of flow-induced forces on the spheres.

Note that we used the angle ψ extracted from Schlieren experiments as input for non-Schlieren experiments. Hence, the actual angle ψ remains unknown. If we had evaluated the Schlieren experiments as detailed as the non-Schlieren experiments, larger uncertainties would have emerged, as the image analysis cannot clearly distinct between the sphere and its wake. Therefore the sphere position is not properly detected, resulting in errors in path, curvature, velocity, and therefore the forces of the sphere. However, the previous discussion showed that the use of Schlieren data for non-Schlieren experiments is justified and provides excellent agreement between theory and experiment.

4. Discussion

Karamanev and co-workers mention that in their experiments all the light spheres ascended along a helicoidal trajectory. In our experiments, even in repeated trials with spheres of the same diameter, no preferred type of path was observed. Each different path gave a different value for the mean rise velocity, which is the reason for the large scatter in our data for $C_D(Re)$. Karamanev and co-workers probably also had the same problems with non-reproducible paths; they only observed the spheres from one side, so they could not distinguish between zigzag or helix. They observed almost identical path frequencies and pitch (as we do) and concluded that all spheres rise along helices; a conclusion which cannot be drawn from one side view.

It is possible that our small tank, with a height of 0.50 m, was too short, and that if the spheres were allowed to rise over a much longer distance they would eventually end-up following helicoidal paths. Jenny et al. (2004) have recently shown by numerical simulations that the $(G, \rho_s/\rho)$ parameter space may be divided into 'regimes', with distinct characteristics of the 'asymptotic states'. These asymptotic states refer to non-transient paths, i.e., pathes of spheres that have been rising for a sufficiently long time. Our experiments correspond to positions in this parameter space which all lie well within the 'chaotic regime'. Chaotic trajectories are characterized by periods with vigorous excursions in random directions, interrupted by periods in which the motion is seemingly 'smooth' or 'well-behaved'. The examples shown in Figs. 2 and 3 are not the paths that would be expected from the analysis

---

[2] Choosing the arithmetic mean of the two extreme values would give very similar results – 30° is thought to be an order of magnitude estimate.

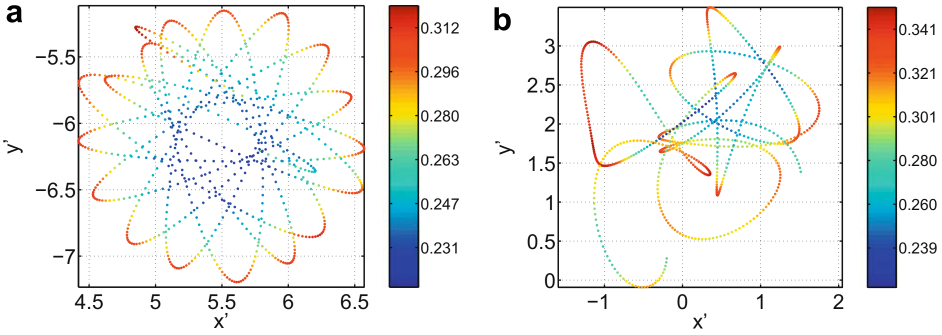

Fig. 10. Projection of the two measured sphere trajectories on the *XY*-plane; origin of frame is located at the position where the spheres enters the water tank. The color values represent the tangential velocity of the spheres, with the numbers next to the color codes giving the corresponding value in ms^{-1}. Spatial coordinates have been non-dimensionalized with the diameter of the spheres. In both cases $\rho_s/\rho \simeq 0.02$. (a) $d = 4.1$ mm, $G = 741$, $Re = 979$; (b) $d = 4.6$ mm, $G = 880$, $Re = 1228$. (For interpretation of the references to color in this figure legend, the reader is referred to the web version of this paper.)

of Jenny et al. (2004) for homogeneous spheres in the chaotic regime; the paths are more 'erratic' and less reproducible. To investigate the effect of the length of the water tank the experiments with light polystyrene spheres are also conducted in a larger water tank (diameter 16 cm, height 2.5 m). We still observed all kinds of trajectories; Fig. 10 shows the reconstructed top views of two representative experiments. It is possible that the lack of reproducibility is due to small imperfections of the polystyrene spheres. They are made by expanding polystyrene with air, which destroys the homogeneity of the sphere. Jenny et al. (2004) performed numerical experiments which show that a small inhomogeneity of the sphere's mass distribution causes the sphere to move in an erratic path, whereas a homogeneous sphere follows a path which is well predicted by their numerical results (see their figures 30 and 31). A second reason for the lack of reproducibility might be the still rather limited field of view (some 100 sphere diameters). This does not enable us to fully characterize the onset of the chaotic behavior as Jenny et al. (2004) did in their numerical work.

The drag coefficient for these experiments in the large tank, as calculated from (5), are also given in Fig. 1 in black; clearly there is no difference with the spheres rising in the small tank. Fig. 11 shows the drag forces experienced by the two spheres, where the vortex angle ψ is again taken to be 30°. We see that our drag model agrees well with the actual drag experienced by the spheres, especially with respect to the phase. We also observe a small deviation in the magnitude of the drag, which is probably due to the lower resolution of the digital data obtained with this setup, resulting in less accurate measurement of the sphere position and therefore velocity. In conclusion, we can say that the drag is properly estimated by the model presented in the previous section for all spheres, irrespective of their non-reproducible and erratic trajectories. The small remaining differences between the measured drag and the modeled drag might be due to a rotation of the sphere; an aspect which has not been addressed in the present investigation, because this rotation could not be determined from the experimental data. Fig. 5 shows that the difference is largest for zigzagging spheres; the sphere might rotate due to sudden changes in the sphere path. Another possibility could be that the angle ψ changes considerable during the sharp turns. Future research should focus on this aspect to improve our model for drag.

Our results can be interrelated with recent numerical findings of Mougin and Magnaudet (2006) on oblate ellipsoidal bubbles rising in water. They propose a similar approach to estimate the drag, where the viscous contribution is based on a calculation of the rate of dissipation in a potential flow (Levich drag). They find that the actual drag experienced by a spiraling bubble consists for 30% of lift-induced drag; we find lift-induced drag percentages between 21% and 26% of the actual drag. Hence, although the mechanism for vorticity production, and therefore the amount of vorticity, is different for a sphere and a bubble the influence of the induced drag on the actual drag is similar. Mougin and Magnaudet (2006) also observed that for ellipsoidal bubbles rising along a helicoidal trajectory the lift forces in the directions of the normal and the binormal to the path have equal magnitudes. We find the same result for a sphere rising along an approximately helicoidal path (see Fig. 4(e)). Recently, Shew et al. (2006) and Shew and Pinton (2006)

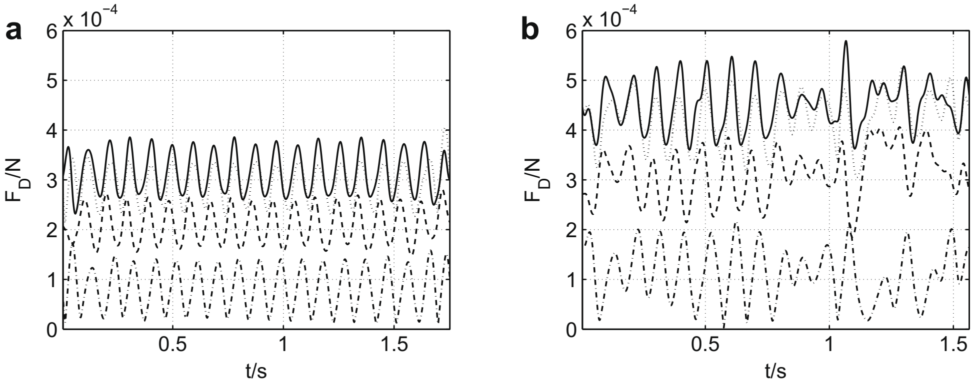

Fig. 11. Solid curves: measured drag force; dashed curves: viscous drag as given by the Turton–Levenspiel relation with the Reynolds number based on the instantaneous velocity; dashed-dotted curves: estimates of the lift-induced drag; dotted curves: drag force as a combination of viscous drag and lift-induced drag. Further details are given in the caption of Fig. 10.

reported that the bubbles in their experiments do not experience a lift-induced drag; contradicting the findings of Mougin and Magnaudet (2006). They state that the actual drag can be modeled by Levich drag with a maximal error of 1%. In our bubble experiments the measured lift-induced drag is similar to that of Mougin and Magnaudet (2006).

Finally, we want to make a remark on a deduction made in de Vries et al. (2002) and Veldhuis et al. (2005), namely, that a pure zigzagging motion of a bubble or a solid sphere is accompanied with a wake that consists of two vortex threads which merge at the centerline of the zigzag and subsequently reappear with reversed direction of the vorticity within the threads. Our results on the lift force show that this needs correction. In Fig. 4(e) it may be seen how the normal component of the lift force on a zigzagging sphere suddenly jumps from a positive value to a negative value, while the magnitude remains the same. This reason for this behavior is that the normal to the path in the Frenet reference frame is directed towards the center of curvature. This forces the normal to change direction; the lift force does not change, it merely changes direction with respect to the normal to the curve. In other words, along the zigzag path points of zero curvature do not correspond to points where the lift force vanishes and changes direction. At the instant that the vortex threads merge no lift is generated, and since the curvature of the path vanishes at the centerline of the zigzag, this would imply a violation of Eq. (15), because the first term on the left-hand side and the term on the right-hand side are zero. What really happens is that at the centerline of the zigzag lift is produced to balance the gravitational force in the direction normal to the zigzag path, while the merging of the threads and the vanishing of the lift occurs some distance away from the centerline. Eq. (15) shows that the value of the gravitational force depends on the density ratio. A density ratio close to one implies a small gravitational force, hence a small lift force. The experiments presented in Veldhuis et al. (2005) used solid spheres with a density close to that of the surrounding fluid, so the error was difficult to detect. But it becomes clear immediately from Fig. 4(e), and in hindsight should have been noticed on inspection of Fig. 2 of de Vries et al. (2002) of a zigzagging gas bubble.

5. Conclusions

By image analysis of stereoscopic recordings of the motion of the light ($\rho_s/\rho \approxeq 0.02$) rising spheres in still water, three-dimensional reconstructions of the trajectories were made, which on further analysis yielded the drag and lift forces experienced by the spheres. Beyond a Reynolds number between $Re = 205.8$ and 211.9 the standard drag curve becomes invalid for these spheres, due to their spiraling. It was proposed that then instead the drag force consists of (i) a viscous contribution that may be estimated from the standard drag curve by evaluating the Reynolds number using the actual value of the velocity, and (ii) an inertial contribution that arises essentially by the same mechanisms that cause the lift-induced drag on airplane wings. Estimates of both contributions, the latter using visualizations of the wakes of the spheres, give a favorable agreement with the measurements. The remaining differences between the measured drag and the modeled drag might be due to a rotation of the sphere; an aspect which has not been addressed in the present investigation, because this rotation could not be determined from the experimental data. Future research should focus on this aspect to improve our model for drag.

There is obviously a connection of our study on freely rising spheres with work done on vortex-induced vibrations, as already exemplified by references to the papers of Lighthill (1986), Leonard and Roshko (2001) and Sarpkaya (2001). This connection is most intimate, perhaps, with studies of the motion of elastically mounted and tethered spheres, an example of which is given in Govardhan and Williamson (2005). Their description of the origin of the lift force on the spheres is essentially similar to what has been put forward by our group in the context of freely rising gas bubbles and solid spheres. It would be interesting to try to combine their beautiful visualizations and DPIV measurements of the sphere wakes with the simple model of the drag force given in Section 3.4. Given the great detail with which the vorticity distributions was characterized, it may even be possible to estimate the vortex-flow forces experienced by the spheres on using the expressions derived by Kambe (1987) and Howe (1995).

Acknowledgements

We thank Andrea Prosperetti, Michel Versluis, and Leen van Wijngaarden for very helpful discussions on both theory and experiment and we kindly acknowledge Harmke van Aken for her contributions to our first experiments on rising light particles. We also thanks Gert-Wim Bruggert and Henni Scholten for invaluable technical support during the experiments. The Lorentz-Center in Leiden is acknowledged for sponsoring the 2005 workshop "Hydrodynamics of bubbly flows" where part of the ideas of this paper emerged. A.B. gratefully acknowledges the CNRS for providing the financial support for a visit at the Laboratoire de Mécanique des Fluides et d'Acoustique at the Ecole Centrale de Lyon, and Michel Lance and Richard Perkins for making the visit such a pleasant one. This work is part of the research programme of the Stichting voor Fundamenteel Onderzoek der Materie (FOM), which is financially supported by the Nederlandse Organisatie voor Wetenschappelijk Onderzoek (NWO).

References

Biesheuvel, A., Hagmeijer, R., 2006. On the force on a body moving in a fluid. Fluid Dyn. Res. 38, 716–742.
Brown, P.P., Lawler, D.F., 2003. Sphere drag and settling velocity revisited. J. Environm. Eng. 129, 222–231.
de Vries, A.W.G., Biesheuvel, A., van Wijngaarden, L., 2002. Notes on the path and wake of a gas bubble rising in pure water. Int. J. Multiphase Flow 28, 1823–1835.
Fernandes, P.C., Ern, P., Risso, F., Magnaudet, J., 2008. Dynamics of axisymmetric bodies rising along a zigzag path. J. Fluid Mech. 606, 15.
Govardhan, R.N., Williamson, C.H.K., 2005. Vortex-induced vibration of a sphere. J. Fluid Mech. 53, 11–47.
Howe, M.S., 1995. On the force and moment on a body in an incompressible fluid, with application to rigid bodies and bubbles at high and low Reynolds numbers. Q.J. Mech. Appl. Math. 48, 401–426.
Jenny, M., Bouchet, G., Dušek, J., 2003. Nonvertical ascension or fall of a free sphere in a Newtonian fluid. Phys. Fluids 15, L9–L12.
Jenny, M., Dušek, J., Bouchet, G., 2004. Instabilities and transition of a sphere falling or ascending freely in a Newtonian fluid. J. Fluid Mech. 508, 201–239.
Johnson, T.A., Patel, V.C., 1999. Flow past a sphere up to a Reynolds number of 300. J. Fluid Mech. 378, 19–70.
Kambe, T., 1987. A new expression of the force on a body in viscous vortex flow and asymptotic pressure field. Fluid Dyn. Res. 2, 15–23.
Karamanev, D.G., 2001. The study of free rise of buoyant spheres in gas reveals the universal behaviour of free rising rigid spheres in fluid in general. Intl J. Multiphase Flow 27, 1479–1486.
Karamanev, D.G., Chavarie, C., Mayer, R.C., 1996. Dynamics of the free rise of a light solid sphere in liquid. AIChE J. 42, 1789–1792.
Karamanev, D.G., Nikolov, L.N., 1992. Free rising spheres do not obey Newton's law for free settling. AIChE J. 38, 1843–1846.
Leonard, A., Roshko, A., 2001. Aspects of flow-induced vibration. J. Fluids Struct. 15, 415–425.
Lighthill, J., 1986. Fundamentals concerning wave loading on offshore structures. J. Fluid Mech. 173, 667–681.
Lunde, K., Perkins, R.J., 1997. Observations on wakes behind spheroidal bubbles and particles. vol. FEDSM97. p. 3530.
Magarvey, R.H., MacLatchy, C.S., 1965. Vortices in sphere wakes. Can. J. Phys. 43, 1649–1656.
Mougin, G., Magnaudet, J., 2002a. The generalized Kirchhoff equations and their application to the interaction between a rigid body and an arbitrary time-dependent viscous flow. Int. J. Multiphase Flow 28, 1837–1851.
Mougin, G., Magnaudet, J., 2002b. Path instability of a rising bubble. Phys. Rev. Lett. 88, 014502.
Mougin, G., Magnaudet, J., 2006. Wake-induced forces and torques on a zigzagging/spiralling bubble. J. Fluid Mech. 567, 185–194.

Sarpkaya, T., 2001. On the force decompositions of Lighthill and Morison. J. Fluids Struct. 15, 227–233.

Schouveiler, L., Provansal, M., 2002. Self-sustained oscillations in the wake of a sphere. Phys. Fluids 14, 3846–3854.

Shew, W.L., Pinton, J.-F., 2006. Dynamical model of bubble path instability. Phys. Rev. Lett. 97, 144508.

Shew, W.L., Poncet, S., Pinton, J.-F., 2006. Force measurements on rising bubbles. J. Fluid Mech. 569, 51–60.

Turton, R., Levenspiel, O., 1986. A short note on the drag correlation for spheres. Powder Technol. 47, 83–86.

Veldhuis, C., Biesheuvel, A., 2007. An experimental study of the regimes of motion of spheres falling or ascending freely in a newtonian fluid. Int. J. Multiphase Flow 33, 1074–1087.

Veldhuis, C.H.J., Biesheuvel, A., van Wijngaarden, L., Lohse, D., 2005. Motion and wake structure of spherical particles. Nonlinearity 18, C1–C8.